Computational Materials Science 123 (2016) 19–25

Contents lists available at ScienceDirect

Computational Materials Science

journal homepage: www.elsevier.com/locate/commatsci

Interatomic potential for the NiTi alloy and its application

Guowu Ren [a,b,*], Huseyin Sehitoglu [b]

[a] Institute of Fluid Physics, China Academy of Engineering Physics, Mianyang 621999, China
[b] Department of Mechanical Science and Engineering, University of Illinois at Urbana-Champaign, Urbana, IL 61801, USA

ARTICLE INFO

Article history:
Received 29 March 2016
Received in revised form 7 June 2016
Accepted 9 June 2016

Keywords:
NiTi
Empirical potential
Ab initio

ABSTRACT

We construct a new interatomic potential for the NiTi alloy, consisting of the previously existing potentials for Ni and Ti and the cross-interaction terms by fitting to *ab initio* or experimental data of several Ni–Ti compounds. This potential correctly reproduces the lattice parameter, cohesive energy and equation of state for B2, B19 and B19′ phases. It also predicts three elastic constants of B2 (austenite) phase matching with experiments and thirteen elastic constants of B19′ (martensite) phase in satisfactory agreement with *ab initio* calculations, which are provided for the first time in comparison with other developed potentials. Additionally, the calculated moduli for B2 and B19′ are in accurate accord with the experimental findings. These good consistencies validate the usefulness of this potential for modeling the martensitic transformation of NiTi alloy induced by temperature or stress control.

1. Introduction

Shape memory NiTi alloy has attracted considerable attentions over a wide range of industrial and commercial applications since it reveals a reversible martensitic transformation induced by temperature or stress [1]. Specifically, transition of NiTi alloy occurs from a cubic B2 structure of high-temperature phase (austenite) to a monoclinic B19′ structure of phase (martensite), accompanying with the distortion and shuffle of crystalline structure. In addition to B2 and B19′ phases validated by experiments, also including the immediate R phase, there exist other intermetallic phases of orthorhombic B19 structure and base-centred orthorhombic (BCO) structure predicted by *ab initio* calculations [2]. The complexity of multiple NiTi phases brings a significant challenge to computational modeling and experimental investigation.

Over the past few years, numerous atomistic modelings of NiTi alloy have mainly concentrated on the prediction of transformation path [3,4], elastic moduli analysis [5,6] and physical mechanism of twinning process of B19′ phase [7] using *ab initio* approaches. However, for these phenomena of plastic deformation [8,9], crack [10,11] with a great amount of atoms, *ab initio* methods restricted to a few hundred atoms or less cannot tackle and large-scale atomistic simulations on the basis of a parameterized semiempirical potential are required. Up to now, such kind of empirical potentials for NiTi alloy are lacking because it needs to reproduce physical properties of both austenite and martensite phases very well. Only the successful potential developed by Lai and Liu [12] is based on tight-binding model in second moment approximation, which predicted a more stable phase of B19′ compared to B2. Recently, Mutter et al. [13] and Zhong et al. [14,15] separately have separately adopted the distinct cut-off function to make the smooth cutoff of this potential for examining the temperature-driven structural phase transition or compressive deformation of NiTi alloy. However, this modified potential for B19′ phase does not predict a shuffle of Ni and Ti atoms reflecting its twinning process and give its very high elastic moduli (see Table 4).

In this work, we present an interatomic potential for NiTi alloy, which exhibits a good description of equilibrium lattice parameter, cohesive energy and energy versus volume relations for B2, B19 and B19′ phases. The calculated elastic properties of B2 and B19′ phases are in good accordance with the experimental or *ab initio* data, which is applied to atomistic simulations of martensitic transformation of NiTi alloy.

2. Procedure for fitted potential

In the current procedure of constructing the many-body potential for binary alloy, we adopt the generalized Finnis–Sinclair (FS) scheme [16] of the total potential energy, written by,

$$E = \sum_{i=1}^{N-1}\sum_{j=i+1}^{N}\phi_{t_i t_j}(r_{ij}) + \sum_{i=1}^{N}F_{t_i}(\bar{\rho}_i) \quad (1)$$

* Corresponding author at: Institute of Fluid Physics, China Academy of Engineering Physics, Mianyang 621999, China.
E-mail address: guowu.ren@yahoo.com (G. Ren).

http://dx.doi.org/10.1016/j.commatsci.2016.06.012
0927-0256/

and

$$\bar{\rho}_i = \sum_j \rho_{t_i t_j}(r_{ij}), \tag{2}$$

where t_i refers to the elemental type of atom i, $\phi_{t_i t_j}(r_{ij})$ is the pair-interaction potential between atom i and j, $F_{t_i}(\bar{\rho}_i)$ is the embedding energy function depending upon the host electron density $\bar{\rho}_i$ induced by all other atoms. The host electron density is obtained by summing the density function $\rho_{t_i t_j}(r_{ij})$ from the atom j. The second term in Eq. (1) stands for the many-body interactions between atoms. With the above formalism for binary alloy, there are totally eight potential functions, where six functions are fitted to predict the properties of pure species and two cross-interaction functions are used for describing the intermetallic compounds. Here the existing potentials are adopted for Ni [17] and Ti [18], of which properties have been illustrated in great detail. Only the cross-interaction terms $\rho_{\mathrm{NiTi}}(r)$ and $\phi_{\mathrm{NiTi}}(r)$ are constructed to match the properties of NiTi alloy, utilizing the following cubic spline form,

$$f(r) = \sum_{i=1}^{N_i} a_i (r_i - r)^3 H(r_i - r). \tag{3}$$

N_i denotes the number of knots. $H(r)$ is the Heaviside step function defined as $H(x) = 1$ for $x \geqslant 0$ and $H(x) = 0$ for $x < 0$. The knot coefficients a_i are the fitting parameters while the knot positions r_i herein keep unchanged. Note that the final position r_i is corresponding with the cutoff radius, denoted as R_c. In current case, we choose the cutoff radius to be $R_c = 0.52$ nm, approaching the value of pure elements (0.5168 nm for Ni [17] and 0.5194 nm for Ti [18]), which lies between fourth nearest neighbor (NN) and fifth NN for the equilibrium B2 structure. Unlike the Lai's potential [12] only covering the second NN ($R_c = 0.42$ nm) and discontinuing at R_c, the choice of this value largely improves the further accuracy of MD simulation and the fitted potential can naturally smooth to be zero at the cutoff site. The total number of the fitting parameters is 22 (8 for $\rho_{\mathrm{NiTi}}(r)$ and 14 for $\phi_{\mathrm{NiTi}}(r)$) as seen in Table 1.

The fitting database for NiTi alloy primarily accounts for energy versus volume (EV) relations for four realistic intermetallic compounds: B2, B19′, B19, BCO and three imaginary compounds (B1-NiTi, $L1_2$-Ni_3Ti and $L1_2$-$NiTi_3$), which are obtained from *ab initio* calculations with Quantum Espresso (QE) [19], a plane-wave DFT code. The previous QE calculations [2,20] with ultrasoft pseudopotentials (USPP) plus generalized gradient approximation (GGA) have offered good descriptions of structural parameters and energy differences among B2, B19, B19′ and BCO phases. We use the same parameter settings for QE as Vishnu et al. [20] to calculate the energies of all structures for about 10 volumes around the equilibrium volume. Since *ab initio* and empirical potential calculations have different reference states, *ab initio* energy $\widetilde{E}$ for a given element or compound $Ni_{1-n}Ti_n$ needs to be shifted to empirical potential energy E according to the following equation,

$$E_{\mathrm{Ni}_{1-n}\mathrm{Ti}_n} = \widetilde{E}_{\mathrm{Ni}_{1-n}\mathrm{Ti}_n} - (1-n)(E_{\mathrm{Ni}} - \widetilde{E}_{\mathrm{Ni}}) - n(E_{\mathrm{Ti}} - \widetilde{E}_{\mathrm{Ti}}), \tag{4}$$

where n represents the concentration of Ti atom, and E_{Ni} and E_{Ti} are the cohesive energies of FCC Ni (Ref. [15]) and HCP Ti (Ref. [16]), respectively. Except for the EV database, three elastic constants (C11, C12 and C44) of B2 NiTi are taken into account, directly gained from the experimental values [21]. With reference to B19′ NiTi, the elastic constants are indirectly expressed as total energy versus deformation strain through QE calculations and currently three terms (C11, C22 and C33) of B19′ are accounted for, including seven *ab initio* energies imposed by the deformation strain. Using the different approaches to involve the elastic constants of B2 and B19′ is that the former [22] has formulated the explicit expressions derived from the known analytical potential while the latter does not. It should be notable that here we do not consider the database of cohesive energy and lattice parameter scaled by the experimental data.

To perform the fitting procedure, an objective function is defined as a least-squares form,

Table 1
Fitting parameters of cross density function ρ_{NiTi} and cross pair function ϕ_{NiTi}.

Term	i	r_i	a_i	i	r_i	a_i
ρ_{NiTi}	1	2.0	−5.7018206539	5	3.4	0.2421738664
	2	2.4	−0.3714021478	6	4.0	−0.0272890386
	3	2.8	−0.3104220976	7	4.6	0.0047470078
	4	3.2	−0.1671834462	8	5.2	0.0017899938
ϕ_{NiTi}	1	2.0	2.9184730067	8	3.3	0.5335512477
	2	2.1	4.1765832294	9	3.6	−0.0779410014
	3	2.2	6.8428168971	10	3.9	−0.0160369303
	4	2.3	11.7153475530	11	4.2	0.0710179537
	5	2.5	2.5532014668	12	4.5	0.0906362468
	6	2.7	3.3956589056	13	4.8	−0.0890091029
	7	3.0	−1.1376598128	14	5.2	−0.0380651928

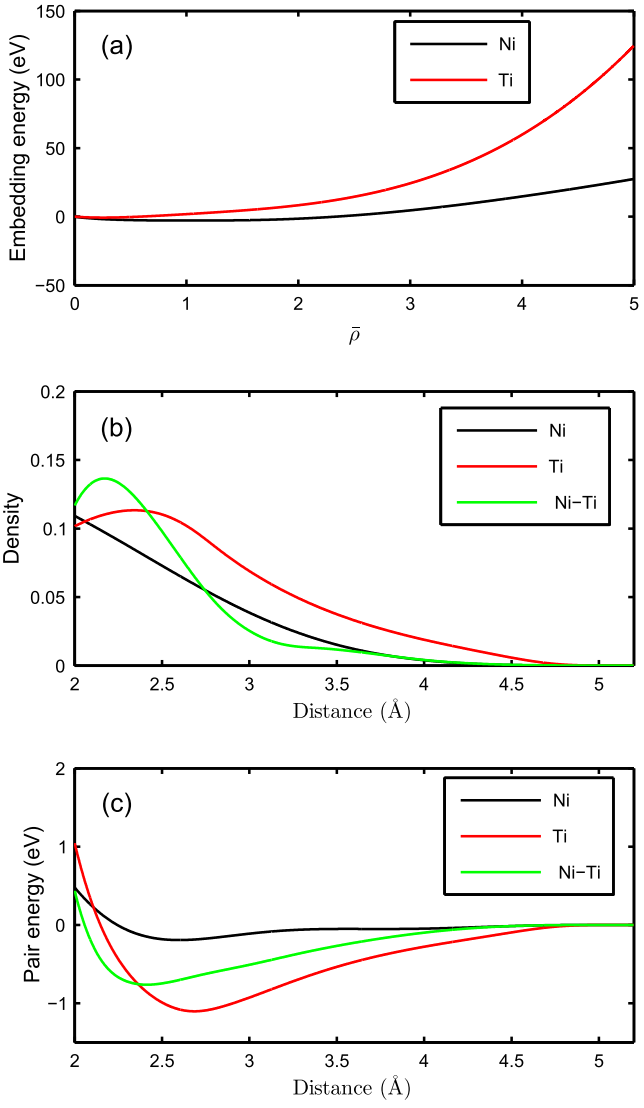

Fig. 1. FS potential functions for NiTi alloy: (a) embedding function, (b) density function and (c) pair function. The potential functions of pure Ni and pure Ti are separately adopted from Refs. [15,16], while the cross density and pair functions are developed in present study.

Table 2
Lattice parameters, volume and cohesive energy (per atom) calculated from the present potential in comparison with the experimental data, *ab initio* calculation (Ref. [27]) and ZGZ potential (Ref. [14]).

Structure	Method	a (Å)	b (Å)	c (Å)	β (deg)	V_0 (Å^3)	E (eV)	$E - E_{B2}$ (meV)
B2	Exp. [25]	3.013			90	27.339		
	Ab initio	3.019			90	27.516		0.0
	ZGZ	3.008			90	27.217	−5.022	0.0
	Present	3.021			90	27.561	−5.079	0.0
B19	Exp. [26]	4.510	4.224	2.899	90	27.614		
	Ab initio	4.633	4.180	2.863	90	27.737		−41
	Present	4.499	4.358	2.878	90	28.210	−5.094	−15
B19′	Exp. [28]	4.646	4.108	2.898	97.78	27.400		
	Ab initio	4.677	4.077	2.917	98.0	27.541		−55
	ZGZ	4.466	4.022	3.005	98.08	26.720	−5.073	−51
	Present	4.606	4.386	2.699	93.41	27.219	−5.108	−29

$$Z = \sum_{i=1} w_i (Y_i(r, a_i) - Y_{i0})^2, \tag{5}$$

where w_i is the fitting weight of different terms, $Y_i(r, a_i)$ is the fitting value related to the adjustable parameters (a_i) and Y_{i0} is the target value (energy or elastic constant). The weight w_i is manually set depending on the importance of the target values, such as, $w = 50$ for EV relation of B2 or B19′ NiTi and $w = 0.25$ for the imaginary compounds. Here we minimize the objective function through the use of downhill simplex method, only requiring function evaluations not derivatives. It should be mentioned that the minimization technique implemented here is in search of local minima. Thus the introduction of the initial parameters constructing the simplex is of great importance. To better initialize the fitting parameters, the cross functions are estimated in advance, where ρ_{NiTi} has an exponential decay, similar to the density function of pure Ni and ϕ_{NiTi} approximates to be alloy potential in light of the alloy model [23].

The optimized fitting parameters are listed in Table 1 and plots of all the potential functions are shown in Fig. 1. Since during the minimization process the fitting procedure does not consider the relaxation of cell parameter and atomic coordinates, the ultimate basic properties of all the structures are calculated using LAMMPS software [24] after tabulating the above functions into FS format. For the sake of comparison with the present fitted potential throughout the paper, the potential improved by Zhong et al. [14] (referred to as the ZGZ potential) is employed in tabular form. Note that in spite of database of seven Ni–Ti compounds being chosen as the fitting targets, here we place an emphasis on the findings of B2, B19 and B19′ phases as will be discussed below.

3. Results and discussions

The calculated equilibrium lattice parameter, volume, cohesive energy and energy difference relative to B2 structure for B2, B19 and B19′ phases at 0 K are listed in Table 2, also including experimental data, *ab initio* data (mainly adopted from Hatcher et al. [27]) and ZGZ potential [14] for the whole comparison, and their crystal structures are viewed in Fig. 2. Seen from Table 2, the present potential for B2 phase gives its lattice constant of $a = 3.021$ Å calculated from EV relation, close to the *ab initio* value of $a = 3.019$ Å; however, it is a slightly larger than the experimental value of $a = 3.013$ Å at 300 K obtained by Sittner [25] and the predicted value of $a = 3.008$ Å by the ZGZ potential. The B19 phase is an intermediate orthorhombic structure without a monoclinic distortion between B2 and B19′ when it is alloyed with Cu from experimental observation. The predicted lattice constants of B19 phase by the present potential are in good agreement with experimental results, separately underestimating a and c by 0.2% and 0.7%, overestimating b by 3.2%. But B19 structure are not provided in the ZGZ potential. For the low-temperature martensitic B19′ phase, its lattice properties have been well understood in experiments. In contrast to the experimental data [28], its lattice parameters herein have the underestimated values of a by 0.8%, c by 6.8% and β by 4.5% and an overestimated value of b by 6.7%, respectively. The ZGZ potential displays the better predicted values of B19′. It should be mentioned that the monoclinic angle of B19′ phase in the framework of *ab initio* calculations is unstable and lattice parameters are obtained by fixing $\beta = 98^\circ$ during the structural optimization while this value has been confirmed from experimental examinations [1,5,6,28].

After analyzing the aforementioned lattice parameters, we turn attention to their cohesive energies evaluated at equilibrium position, representing their structural stability. Seen from Table 2, the cohesive energy of B2 structure given by the present potential shows $E = -5.079$ (eV/atom), which is lower than that of the ZGZ potential ($E = -5.022$ (eV/atom)). By choosing E_{B2} as a reference value, the energy differences for B19 and B19′ phases are −15 (meV/atom) and −29 (meV/atom), respectively, which reveals a decreasing tendency as same as that of *ab initio* calculations [27] despite these values are a little small. But the ZGZ potential [14] only predicted the correct energy difference between B2 and B19′.

Overall, the equilibrium lattice parameters and cohesive energies for B2, B19 and B19′ phases on the basis of the present empirical potential display a reasonable agreement with *ab initio*

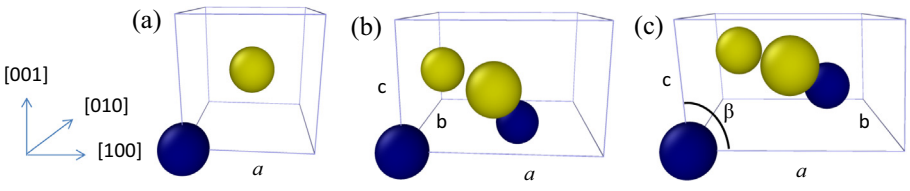

Fig. 2. Crystal structures of NiTi obtained from the present potential: (a) B2; (b) B19; (c) B19′, where blue and yellow represent Ti and Ni atoms, respectively. The lattice parameters *a*, *b* and *c* are denoted separately along the [100], [010] and [001] directions. (For interpretation of the references to colour in this figure legend, the reader is referred to the web version of this article.)

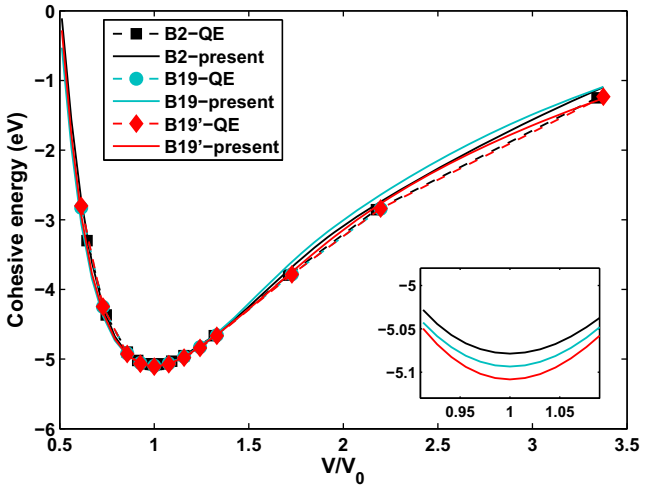

Fig. 3. Comparisons of EV relations between the present potential (solid line) and QE calculation (dot line) for B2, B19 and B19′ structures. For the sake of convenient comparison together, atomic volume is scaled by equilibrium volume V_0 and QE energies are shifted by the amount, an energy difference of B2 structure at equilibrium site.

Table 3
Comparison of atomic positions for B19′ structure, expressed as the conventional coordinates. There are four atoms per unit cell shown in the viewing frame, where blue denotes Ti atom and yellow is for Ni atom.

Method	Ti	Ni	Structure
Exp. [28]	0,0,0 0.5672,0.5,0.1648	0.4588,0,0.6196 0.1084,0.5,0.5452	
Ab initio [2]	0,0,0 0.5626,0.5,0.1708	0.4558,0.0,0.6304 0.1067,0.5,0.5404	
ZGZ [14]	0,0,0 0.5,0.5,0.0	0.5,0.0,0.5 0.0,0.5,0.5	
Present	0,0,0 0.6973,0.5,0.3413	0.4906,0,0.6645 0.2067,0.5,0.6768	

or experimental data. Compared to the ZGZ potential, an important intermediate B19 phase playing a significant role in understanding B2–B19′ transformation path [3], is firstly included and its basic properties are very well fitted. The energy differences among these phases predict the correct structural stability matching with the experimental observations and *ab initio* findings. These small values just mark the occurrence of martensitic transformation for materials. However, some big discrepancies emerge, especially for lattice constants b, c and monoclinic angle β of B19′ phase while its equilibrium volume is in excellent agreement with the experiment. This also implies that the potential energy surface of B19′ is more complicated than that of B2, not being accurately predicted through simple EV database.

Fig. 3 compares the EV relations (equation of state) for B2, B19 and B19′ structures obtained by the present potential and QE calculations, with volume spanning from 0.5 V_0 to 3.5 V_0. To facilitate the comparison together, the volume is scaled with the equilibrium volume V_0 and all the QE energies are shifted by the same amount, an energy difference of B2 structure at equilibrium site. Good agreement in the overall plot is revealed between two calculated methods and the difference among the phases is quite small, which is clearly depicted in the inset of Fig. 3. Nevertheless, it is carefully observed that there remain some small deviations in the expansion region of EV plot.

For monoclinic B19′ structure, atomic position within the unit cell is also an important parameter to essentially be determined. In Table 3 we comparatively display the atomic positions of B19′ structure from experimental data [28], *ab initio* calculations [2], ZGZ potential [14] and the present potential, expressed as the conventional coordinates including four atoms (2 Ni and 2 Ti) per unit cell. The *ab initio* results performed by QE calculations are close to the experimental ones, also chosen upon construction of B19′ structure during the fitting procedure. It is clearly found from experimental and *ab initio* data that the distribution of atomic positions has a slight distortion while the ZGZ potential indicates the fractional coordinates of four atoms positioned equivalent to the face-centered cubic structure. The current atomic positions optimized with the present potential are similar to the experimental and *ab initio* cases. This kind of atom arrangement represents a

Table 4
Calculated elastic constants and moduli for B2 and B19′ structures (in GPa; except ν, dimensionless).

	B2				B19′				
	Exp.[a]	*Ab initio*[b]	ZGZ[c]	Present	*Ab initio*[a]	*Ab initio*[d]	*Ab initio*[e]	ZGZ	Present
C11	162	183	205	146	249	223	238	303	218
C12	129	146	136	122	129	129	139	222	120
C13					107	99	102	326	103
C15					15	27	27	175	−16
C22					245	241	234	1135	252
C23					125	125	114	400	72
C25					−3	−9	−7	125	−7
C33					212	200	209	692	206
C35					−1	4	1	292	2
C44	35	46	47	35	87	76	77	286	37
C46					−4	−4	−5	110	−2
C55					66	21	23	215	41
C66					86	77	72	114	43
B	140	158	159	130	159	152	154	447	141
G	28	35	42	26	71	56	56	202	50
E	78	98	116	73	185	149	150	526	133
ν	0.41	0.40	0.38	0.41	0.31	0.34	0.34	0.30	0.34

[a] Ref. [21].
[b] Ref. [27].
[c] Ref. [14].
[d] Ref. [29].
[e] Ref. [30].

Table 5
Three compliance constants (in 10^{-3} GPa^{-1})) and direction-dependent moduli (in GPa) of B19′ structure, compared to the experimental and *ab initio* data.

	Exp. [6]	*Ab initio* [27]	*Ab initio* [29]	Present
S11	11.5	6.04	9.78	7.66
S22	13.4	6.75	9.0	5.42
S33	10.6	7.21	7.8	6.50
$E_{(100)}$	101.4	177.4	146.2	125.1
$E_{(010)}$	74.4	148.1	111.1	184.4
$E_{(001)}$	94.4	138.7	128.2	153.8

shuffle mode between Ni and Ti atoms, which easily achieves a mirror reflection to form the twinning structure. However, atoms Ti and Ni at the fractional coordinate of $y = 0.5$ shift by a displacement in comparison with the experimental data.

For NiTi alloy with shape memory effect, elastic property determination of B2 and B19′ phases is vital to investigate its mechanical behavior, particularly for the latter which elastic moduli are a focus of the recent experimental study [5,6]. Employing the present potential, we calculated the elastic constants of such two structures in comparison with the experimental data, *ab initio* results and ZGZ potential, shown in Table 4, where B2 phase has three independent elastic constants and B19′ phase has thirteen ones. The calculated procedures of elastic constants as well as elastic moduli, have been detailed in these literatures [27,29,30]. Note that up to now elastic constants of only B2 phase at finite temperature have been experimentally reported, shown in first row of Table 4 obtained by Mercier et al. [21] at 298 K. Our calculated values of C12 and C44 are in close to the experiment while C11 is smaller by 9.8%, and these values are underestimated from *ab initio* data. With respect to B19′ phase, effort of elastic constants only centered on *ab initio* data via all-electron potential method [27] or ultrasoft pseudopotential [29,30]; however, the results between them are close. It should be noted that the elastic constants of B19′ phase with the ZGZ potential are not shown in the original paper [14]. Here we recalculate these values and find large deviations from *ab initio* data. In contrast, most of values predicted by the present potential are very well reproduced, except that herein C15 is negative, and C44 and C66 are only half of those calculated with *ab initio* approach.

In spite of the unavailable experimental data about elastic constants of B19′, there have been several measured direction-dependent Young's moduli through the use of *in situ* neutron diffraction technique [5,6]. Using the elastic constants of B19′ listed in Table 4, the direction-dependent moduli $E_{(hkl)}$ in direction perpendicular to the *hkl* plane for monoclinic crystal [31] could be determined from

$$\begin{aligned} E_{(hkl)} = {} & l_1^4 s_{11} + 2l_1^2 l_2^2 s_{12} + 2l_1^2 l_3^2 s_{13} + 2l_1^3 l_3 s_{15} + l_2^4 s_{22} + 2l_2^2 l_3^2 s_{23} \\ & + 2l_1 l_2^2 l_3 s_{25} + l_3^4 s_{33} + 2l_1 l_3^3 s_{35} + l_2^2 l_3^2 s_{44} + 2l_1 l_2^2 l_3 s_{46} \\ & + l_1^2 l_3^2 s_{55} + l_1^2 l_2^2 s_{66}, \end{aligned} \tag{6}$$

where l_1, l_2 and l_3 are the direction cosines and s_{ij} are compliance constants inverse to elastic constants. In Table 5, the direction-dependent moduli $E_{(100)}, E_{(010)}, E_{(001)}$ in terms of the present potential are calculated, which are of a same order of magnitude compared with *ab initio* results while larger than the experimental ones owing to the measurement for polycrystalline B19′ NiTi. But careful examination finds that direction-dependent moduli here in three primary planes have a distinct sequence in value from the experimental case while *ab initio* results in Ref. [29] accords with the trend. This discrepancy originates from the lower value of non-diagonal elastic constants in Table 4. Additionally, to fully

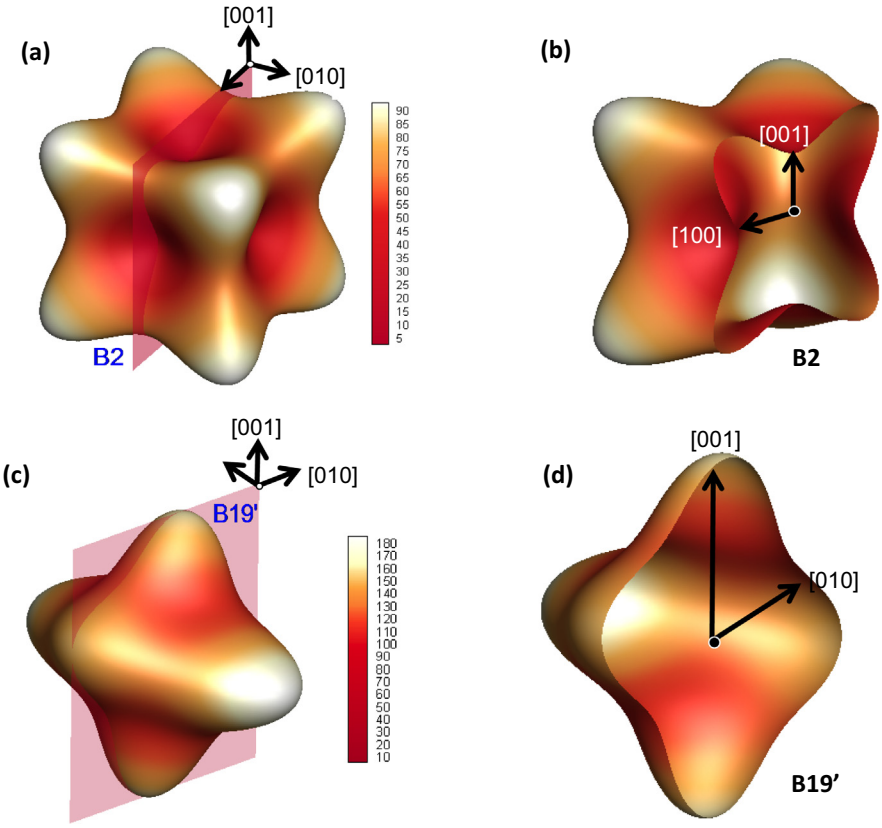

Fig. 4. Representation surfaces of direction-dependent elastic moduli for B2 and B19′: (a) B2; (b) cut view of B2; (c) B19′; (d) cut view of B19′.

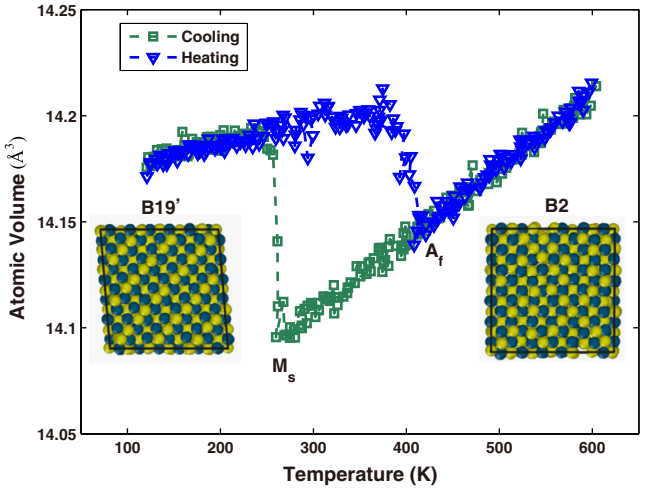

Fig. 5. Temperature-driven phase transformation between B2 and B19′ phases, where an atomic volume is changed as the temperature. The temperature control is imposed firstly by cooling (green plot) from 600 K to 120 K and then by heating (blue plot) to 600 K. (For interpretation of the references to colour in this figure legend, the reader is referred to the web version of this article.)

characterize the anisotropic behavior of B19′, we plot the complete and cut representation surface of direction-dependent moduli in Fig. 4(c) and (d), also including cubic B2 crystal in Fig. 4(a) and (b).

Using Voigt formalism, we obtain the bulk (B), shear (G) and Young's (E) moduli, and Poisson's ratio (μ) calculated from the elastic constants (see Table 4), which are in good agreement separately comparing the values of the present potential with experimental or *ab initio* data for B2 and B19′ phases. As for B19′ phase, experimentally our calculation on Young's modulus of 133 GPa is accurately consistent with the average modulus of 134 GPa [5], but larger than that of 66.7 GPa [6]. In spite of small difference of bulk modulus between two phases, shear and Young's moduli both increase significantly from B2 to B19′, which further confirms the feasibility of martensitic transformation as proposed in the Müller–Achenbach–Seelecke model [32].

To further assess the ability of this empirical potential in studying the dynamic property of NiTi alloy, we conduct the molecular dynamics simulations of phase transformation using LAMMPS. Fig. 5 displays the temperature-driven phase transformation where an atomic volume is changed as the temperature. The simulated supercell with B2 structure consists of 864 atoms and periodic boundary conditions are imposed along three directions. The system is initially equilibrated at 600 K. Then the temperature is reduced from 600 K to 120 K and increases again up to 600 K. During cooling and heating process, the atomic volume is calculated, shown in Fig. 5. Seen from this figure, a sharp jump of the atomic volume signifies the phase transformation between high-temperature B2 austenite phase and B19′ martensite phase. The corresponding sites are M_s temperature of ~260 K and A_f temperature of ~417 K, which separately are slightly lower and higher than the experimental values [5] of $M_s \sim 344$ K and $A_f \sim 382$ K. The atomic volume change between B19′ and B2 phases at room temperature is 0.64%, being a small value which agrees with the experimental measurements [33]. As for stress-driven phase transformation, superelasticity of the NiTi crystal is also captured under compression or tension loads. When transforming from B2 to B19′, the transform stress level, the stress hysteresis and the transform stress as a function of temperature are in general agreement with the experiments. The details could be found in our recently-published literature [34], which is not described here. Therefore, it is clearly indicated from our simulations that the present potential can be appropriate for investigating the temperature-driven as well as stress-induced martensitic transformation of NiTi alloy.

4. Conclusions

In this work we have developed a semiempirical potential with FS formalism for NiTi alloy through fitting to a large set of the calculated energies and elastic constants obtained from *ab initio* or experiment. In contrast to other potentials, the present potential makes a better fit to basic properties for B2, B19 and B19′ NiTi. The calculated energy differences of these three phases give a correct tendency of characterizing the crystal stability, which is in reasonable agreement with *ab initio* calculations. The EV relations obtained from this potential match very well with QE calculations, in which the volume ranges from 0.5 V_0 to 3.5 V_0, indicating a good description of structural states far from the equilibrium site. Of most importance is that elastic properties of both B2 and B19′ phases are accurately determined compared to the experimental or *ab initio* findings, and firstly given because to date there are not any empirical potentials producing the reliable elastic constants and moduli of B19′. Thus the present potential reproduces the main properties for B2 and B19′ structures, which is capable of investigating the dynamic phase transformation of NiTi alloy. However, we also note that some results are slightly larger or smaller in comparison with *ab initio* data, such as, lattice constants b and c of B19′ phase, and its elastic constants C44, C55 and C66. The discrepancy indicates that the utilized fitting database, including the more complicated configurations, need to be greatly increased and only accounting for EV database is not sufficient, which is an ongoing work.

Acknowledgments

This work was done while G.W. Ren was a visiting scholar in UIUC. We thank Avinesh Ojha for drawing the three-dimensional representation surface. H. Sehitoglu gratefully acknowledges Nyquist Chair funds. We also acknowledge the use of Taub cluster at UIUC.

References

[1] K. Otsuka, X. Ren, Prog. Mater. Sci. 50 (2005) 511–578.
[2] X. Huang, G.J. Ackland, K.M. Rabe, Nat. Mater. 2 (2003) 307–311.
[3] S. Kibey, H. Sehitoglu, D.D. Johnson, Acta Mater. 57 (2009) 1624–1629.
[4] N. Hatcher, O. Yu. Kontsevoi, A.J. Freeman, Phys. Rev. B 79 (2009) 020202(R).
[5] S. Qiu, B. Clausen, S.A. Padula II, R.D. Noebe, R. Vaidyanathan, Acta Mater. 59 (2011) 5055–5066.
[6] A.P. Stebner, D.W. Brown, L.C. Brinson, Appl. Phys. Lett. 102 (2013) 211908.
[7] T. Ezaz, H. Sehitoglu, H.J. Maier, Acta Mater. 59 (2011) 5893–5904.
[8] J. Pfetzing-Micklish, C. Somsen, A. Dlouhy, C. Begau, A. Hartmaier, M.F.-X. Wagner, G. Eggeler, Acta Mater. 61 (2013) 602–6161.
[9] O. Benafan, R.D. Noebe, S.A. Padula II, A. Garg, B. Clausen, S. Vogel, R. Vaidynanathan, Int. J. Plast. 51 (2013) 103–121.
[10] S. Gollerthan, M.L. Young, A. Baruj, J. Frenzel, W.W. Schmahl, G. Eggeler, Acta Mater. 57 (2009) 1015–1025.
[11] M.L. Young, S. Gollerthan, A. Baruj, J. Fenzel, W.W. Schmahl, G. Eggeler, Acta Mater. 61 (2013) 5800–5806.
[12] W.S. Lai, B.X. Liu, J. Phys.: Condens. Matter 12 (2000) L53–L56.
[13] D. Mutter, P. Nielaba, Phys. Rev. B 82 (2010) 224201.
[14] Y. Zhong, K. Gall, T. Zhu, J. Appl. Phys. 110 (2011) 033532.
[15] Y. Zhong, K. Gall, Ting Zhu, Acta Mater. 60 (2012) 6301–6311.
[16] M.I. Mendelev, D.J. Sordelet, M.J. Kramer, J. Appl. Phys. 102 (2007) 043501.
[17] Y. Mishin, Acta Mater. 52 (2004) 1451–1467.
[18] R.R. Zope, Y. Mishin, Phys. Rev. B 68 (2003) 024102.
[19] P. Giannozzi, S. Baroni, et al., J. Phys. Condens. Matter 21 (2009) 395502.
[20] K.G. Vishnu, A. Strachan, Phys. Rev. B 85 (2012) 014114.
[21] O. Mericer, K.N. Melton, G. Gremaud, J. Hägi, J. Appl. Phys. 51 (1980) 1833.
[22] Y. Mishin, Handbook of Materials Modeling, in: S. Yip (Ed.), Springer, Dordrecht, The Netherlands, 2005, pp. 459–478.
[23] R.A. Johnson, Phys. Rev. B 39 (1989) 12554–12559.
[24] S.J. Plimpton, J. Comp. Phys. 117 (1995) 1–19.
[25] P. Sittner, P. Lukás, D. Neov, V. Novák, D.M. Toebbens, J. Phys. IV France 112 (2003) 709–712.

[26] T. Nam, T. Saburi, Y. Nakata, S. Shimizu, Mater. Trans., JIM 31 (1990) 1050–1056.
[27] N. Hatcher, O. Yu. Kontsevoi, A.J. Freeman, Phys. Rev. B 80 (2009) 144203.
[28] Y. Kudoh, M. Tokonami, S. Miyazaki, K. Otsuka, Acta Metall. Mater. 33 (1985) 2049–2056.
[29] M.F.-X. Wagner, W. Windl, Acta Mater. 56 (2008) 6232–6254.
[30] J. Wang, H. Sehitoglu, Int. J. Plast. 61 (2014) 17–31.
[31] J.Y. Nye, Physical Properties of Crystals, Clarendon Press, Oxford, 1957.
[32] M. Achenbach, Int. J. Plast. 5 (1989) 371–395.
[33] S.D. Prokoshkin, A.V. Korotitskiy, V. Brailovski, S. Turenne, I. Yu. Khmelevskaya, T.B. Trubitsyna, Acta Mater. 52 (2004) 4479–4492.
[34] P. Chowdhury, G. Ren, H. Sehitoglu, Phil. Magn. Lett. 95 (2015) 574–586.